J. Fluid Mech. (2006), *vol.* 562, *pp.* 383–403.
doi:10.1017/S0022112006001121 Printed in the United Kingdom

Group analysis, direct numerical simulation and modelling of a turbulent channel flow with streamwise rotation

By M. OBERLACK[1], W. CABOT[2,3], B. A. PETTERSSON REIF[4] AND T. WELLER[1]

[1]Department of Mechanical Engineering, Technische Universität Darmstadt, Petersenstraße 13, D-64287 Darmstadt, Germany

[2]Center for Turbulence Research, Stanford University, Stanford, CA 94305, USA

[3]UC/LLNL, PO Box 808, L-22, Livermore, CA 94551, USA

[4]Norwegian Defence Research Establishment (FFI), NO-2027 Kjeller, Norway

(Received 26 May 2004 and in revised form 5 February 2006)

The turbulent channel flow with streamwise rotation has been investigated by means of several different analytical, numerical, and modelling approaches. Lie group analysis of the two-point correlation equations led to linear scaling laws for the streamwise mean velocity. In addition it was found that a cross-flow in the spanwise direction is induced, which may also exhibit a linear region. By further analysis of the two-point correlation equation, it is shown that all six components of the Reynolds stress tensor are non-zero. In addition certain symmetries and skew-symmetries about the centreline have been established for all flow quantities. All these findings of the analysis have been verified very well by means of direct numerical simulations (DNS). The flow has also been calculated with large-eddy simulations (LES) and second-moment closure models. The dynamic LES captured most of the theoretical and DNS findings quantitatively. Except for one stress component the second-moment closure model was able to capture most of the basic trends, but no quantitative agreement could be achieved.

1. Introduction

During the development of the symmetry approach in Oberlack (2001), it was noticed that there may be one additional turbulent scaling law which was not mentioned since no experimental or direct numerical simulation (DNS) data were available. This concerns the turbulent channel flow rotating about the streamwise direction. A sketch of the flow geometry is given in figure 1.

The flow appears to have several common features with the classical rotating channel flow (Johnston, Halleen & Lazius 1972) but also has some very distinct characteristics. The classical case considers the rotation of a turbulent channel flow about the spanwise direction (x_3). In this flow the mean streamlines follow plane spirals. In contrast to this, mean streamlines of the present flow exhibit corkscrew-like spirals. However, the most obvious difference between the two cases may be the induction of a mean velocity in the x_3-direction. This cross-flow can be deduced by investigating the mean momentum equation and the Reynolds stress transport

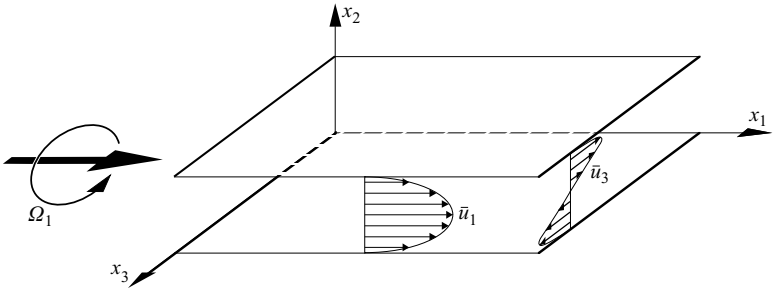

FIGURE 1. Sketch of the flow geometry of a turbulent channel flow with streamwise rotation.

equation. It is interesting to note that the induced cross-flow is a property of the turbulent flow and may not be deduced from the equations for laminar flows.

Similarly to the classical case, it will be shown that the only self-similar mean velocity profiles are linear functions,

$$\bar{u}_1 = A_1 \Omega_1 x_2 + B_1 \quad \text{and} \quad \bar{u}_3 = A_2 \Omega_1 x_2 + B_2, \tag{1.1}$$

to be derived in the subsequent sections. In both the present and the classical case, the mean velocities scale on the rotation rate.

Nevertheless, it is anticipated that the general appearance of the mean velocity profile in the x_1-direction is very different from the classical case. Since the reflection symmetry about the centreline is not broken, the mean velocity may stay symmetrical. In Oberlack (2001) it was observed that, except for the log-law, the highest degree of symmetry is usually obtained in flow regions with the weakest wall influence. Hence, it is expected that two linear regions may emerge near the centre region.

The paper is organized as follows. In the next section three different analyses are presented. The one which initiated the project is Lie group analysis of the present flow, which suggested the linear velocity profiles. Besides that analysis, global time scales of the flow will be investigated which indicate the location of the linear regions. In the final analysis, the symmetry of flow quantities about the centreline of the channel will be examined. In § 3, a DNS of the rotating channel flow is presented. Mean velocities and statistical quantities for different rotation rates will be established. Finally, the present test case is calculated with turbulence models. Results from second-moment closure models and large-eddy simulations (LES) are shown.

2. Analysis

The basis for the analysis of the present flow geometry in §§ 2.2 and 2.3 is the mean momentum equation and the two-point velocity correlation equation in a rotating frame of reference. Assuming the mean velocity parallel to the walls as shown in figure 1 and all stresses only depending on x_2 we obtain

$$0 = -\frac{1}{\rho}\frac{\partial \bar{p}}{\partial x_1} - \frac{\partial \overline{u_1 u_2}}{\partial x_2} + \nu \frac{\partial^2 \bar{u}_1}{\partial x_2^2}, \tag{2.1a}$$

$$0 = -\frac{1}{\rho}\frac{\partial \bar{p}}{\partial x_2} - \frac{\partial \overline{u_2 u_2}}{\partial x_2} - 2\Omega_1 \bar{u}_3, \tag{2.1b}$$

$$0 = -\frac{\partial \overline{u_2 u_3}}{\partial x_2} + \nu \frac{\partial^2 \bar{u}_3}{\partial x_2^2}, \tag{2.1c}$$

and

$$
\begin{aligned}
0 = &-R_{2j}\delta_{i1}\frac{\mathrm{d}\bar{u}_1(x_2)}{\mathrm{d}x_2} - R_{2j}\delta_{i3}\frac{\mathrm{d}\bar{u}_3(x_2)}{\mathrm{d}x_2} - R_{i2}\delta_{j1}\frac{\mathrm{d}\bar{u}_1(x_2+r_2)}{\mathrm{d}(x_2+r_2)} - R_{i2}\delta_{j3}\frac{\mathrm{d}\bar{u}_3(x_2+r_2)}{\mathrm{d}(x_2+r_2)} \\
&- [\bar{u}_1(x_2+r_2) - \bar{u}_1(x_2)]\ \frac{\partial R_{ij}}{\partial r_1} - [\bar{u}_3(x_2+r_2) - \bar{u}_3(x_2)]\ \frac{\partial R_{ij}}{\partial r_3} \\
&- \frac{1}{\rho}\left[\delta_{i2}\frac{\partial \overline{pu_j}}{\partial x_2} - \frac{\partial \overline{pu_j}}{\partial r_i} + \frac{\partial \overline{u_i p}}{\partial r_j}\right] + \nu\left[\frac{\partial^2 R_{ij}}{\partial x_2 \partial x_2} - 2\,\frac{\partial^2 R_{ij}}{\partial x_2 \partial r_2} + 2\,\frac{\partial^2 R_{ij}}{\partial r_k \partial r_k}\right] \\
&- \frac{\partial R_{(i2)j}}{\partial x_2} + \frac{\partial}{\partial r_k}\left[R_{(ik)j} - R_{i(jk)}\right] - 2\,\Omega_1[e_{1li}R_{lj} + e_{1lj}R_{il}]
\end{aligned}
\tag{2.2}
$$

(see e.g. Rotta 1972; Hinze 1987); $\bar{u}_i$, $\bar{p}$, $\overline{u_i u_j}$, ν, Ω_1, and e_{ijk} are respectively the mean velocity, the mean pressure, the Reynolds stress tensor, the dynamic viscosity, the rotation rate in the x_1-direction, and the alternation tensor. The five two-point correlation tensor functions which appear in equation (2.2) are defined as

$$
R_{ij}(\boldsymbol{x}, \boldsymbol{r}; t) = \overline{u_i(\boldsymbol{x}, t)\, u_j\big(\boldsymbol{x}^{(1)}, t\big)}, \tag{2.3a}
$$

$$
\overline{pu_j}(\boldsymbol{x}, \boldsymbol{r}; t) = \overline{p(\boldsymbol{x}, t)\, u_j\big(\boldsymbol{x}^{(1)}, t\big)}, \quad \overline{u_j p}(\boldsymbol{x}, \boldsymbol{r}; t) = \overline{u_j(\boldsymbol{x}, t)\, p\big(\boldsymbol{x}^{(1)}, t\big)}, \tag{2.3b}
$$

and

$$
\left.
\begin{aligned}
R_{(ik)j}(\boldsymbol{x}, \boldsymbol{r}; t) &= \overline{u_i(\boldsymbol{x}, t)\, u_k(\boldsymbol{x}, t)\, u_j\big(\boldsymbol{x}^{(1)}, t\big)}, \\
R_{i(jk)}(\boldsymbol{x}, \boldsymbol{r}; t) &= \overline{u_i(\boldsymbol{x}, t)\, u_j\big(\boldsymbol{x}^{(1)}, t\big)\, u_k\big(\boldsymbol{x}^{(1)}, t\big)},
\end{aligned}
\right\} \tag{2.3c}
$$

where u_i and p correspond to the fluctuating quantities. The tensors (2.3*a*)–(2.3*c*) are functions of the physical and the correlation space coordinates $\boldsymbol{x}$ and $\boldsymbol{r} = \boldsymbol{x}^{(1)} - \boldsymbol{x}$ respectively. For the present case all statistical quantities depend only on the wall-normal coordinate x_2 and the correlation coordinate $\boldsymbol{r}$. The double two-point correlation tensor R_{ij}, hereafter simply referred to as two-point correlation, converges to the Reynolds stress tensor $\overline{u_i u_j}$ in the limit of zero separation $|\boldsymbol{r}|$:

$$
\overline{u_i u_j}(\boldsymbol{x}) = \lim_{r \to 0} R_{ij}(\boldsymbol{x}, \boldsymbol{r}). \tag{2.4}
$$

It should be noted that the two-point correlation equation only contains the triple correlations as unknown terms. For both two-point velocity–pressure correlations, $\overline{u_i p}$ and $\overline{pu_j}$ a Poisson equation may be derived (see e.g. Oberlack 1994, 1995). In addition, all dependent variables in equation (2.2) must satisfy the continuity conditions

$$
\frac{\partial R_{ij}}{\partial x_i} - \frac{\partial R_{ij}}{\partial r_i} = 0, \quad \frac{\partial R_{ij}}{\partial r_j} = 0, \quad \frac{\partial \overline{pu_j}}{\partial r_j} = 0, \quad \frac{\partial \overline{u_i p}}{\partial x_i} - \frac{\partial \overline{u_i p}}{\partial r_i} = 0. \tag{2.5}
$$

To help in understanding the self-similarity of the two-point correlation equation given below, two identities may give some interesting insight in the structure of the two-point correlation function. They can easily be derived from a geometrical consideration by interchanging the two points $\boldsymbol{x}$ and $\boldsymbol{x}^{(1)} = \boldsymbol{x} + \boldsymbol{r}$:

$$
R_{ij}(\boldsymbol{x}, \boldsymbol{r}) = R_{ji}(\boldsymbol{x} + \boldsymbol{r}, -\boldsymbol{r}), \quad \overline{u_i p}(\boldsymbol{x}, \boldsymbol{r}) = \overline{pu_i}(\boldsymbol{x} + \boldsymbol{r}, -\boldsymbol{r}). \tag{2.6}
$$

The former is particularly interesting for the trace elements of R_{ij} since it defines a functional equation in real- and correlation-space. There also exists a similar identity to (2.6) for the triple correlation, which will not be utilized here.

Some fundamental properties of the flow can already be seen from the equations (2.1*a*)–(2.1*c*). For high-Reynolds-number flows, viscous transport terms are only significant in the near-wall region. In regions sufficiently far from solid walls,

the viscous terms may be neglected to leading order, and the balance is dominated by the pressure and the turbulent stresses.

From equation (2.1*a*) the usual linear turbulent shear stress profile for $\overline{u_1u_2}$ may be derived because the pressure gradient in the streamwise (x_1) direction is constant. Since no pressure gradient is present in the spanwise (x_3) direction, it can be deduced from equation (2.1*c*) that the shear stress $\overline{u_2u_3}$ is uniform. Equation (2.1*b*) only determines the pressure gradient in the wall-normal direction. Though it is the only mean momentum equation containing the Coriolis force, it has no influence on the mean velocity. It will be seen later that the mean velocity is determined only by the turbulent stresses. This is similar to the usual non-rotating channel flow in which no information on the mean flow can be determined from the mean momentum equation.

At this point it will be anticipated that besides the shear stress $\overline{u_2u_3}$ the additional shear stress $\overline{u_1u_3}$ is induced due to the rotation. This can be taken from equation (2.2) in which a Coriolis term appears in the R_{13}-equation. From the structure of the '13' equation, it appears that the Coriolis term may not be balanced solely by the pressure–velocity correlation and by the triple correlation. One may naturally expect that the term $[\bar{u}_k(x_2+r_2)-\bar{u}_k(x_2)]\,\partial R_{13}/\partial r_k$ may also contribute to the balance in the equation. Hence $\overline{u_1u_3}$ may be non-zero though this stress has no counterpart in the mean velocities in an eddy-viscosity sense.

2.1. *Time-scale analysis*

In the present subsection the characteristic time scales of the viscous sublayer and the universal logarithmic region will be compared with the characteristic time scale of the rotation rate. The latter is defined as

$$t_\Omega \equiv \frac{1}{\Omega} \tag{2.7}$$

where Ω is the rotation rate about the x_1-direction, also denoted by Ω_1.

The characteristic time scale of the viscous sublayer and the universal logarithmic region are

$$t_\nu \equiv \frac{\nu}{u_\tau^2} \quad \text{and} \quad t_{\log} \equiv \frac{x_2}{u_\tau} \tag{2.8}$$

respectively where u_τ is the 'friction velocity' defined as $u_\tau = \sqrt{\nu(\partial\bar{u}_1/\partial x_2)|_{\text{wall}}}$. For sufficiently high Reynolds number, t_ν is a fixed small quantity while $t_{\log}$ increases with the distance from the wall. Comparing the ratio of these flow time scales with the rotation time scale we respectively obtain

$$T_1 = \frac{t_\nu}{t_\Omega} = \frac{\nu\Omega}{u_\tau^2} = \frac{Ro}{2Re_\tau}, \tag{2.9}$$

$$T_2 = \frac{t_{\log}}{t_\Omega} = \frac{x_2\Omega}{u_\tau} = Ro\frac{x_2}{h}, \tag{2.10}$$

where $Re_\tau = hu_\tau/2\nu$, $Ro = \Omega h/u_\tau$ and h is the channel width.

For zero rotation rate both quantities are exactly zero. However, assuming Ro of $O(1)$ and supposing Re to be a large parameter, the time-scale ratio T_1 is a small quantity. Hence it is concluded that rotation only perturbs the viscous sublayer, and a significant change may not be observed.

Considering the same order of magnitude assumptions for Ro as above, it can be concluded that T_2 may only be a small parameter for small y/h. This is the flow region close to the wall and next to the viscous sublayer. In contrast, if y/h is of $O(1)$, T_2 may become an $O(1)$ parameter. Consequently, we conclude that this is the flow

region which is affected most by the system rotation. In this region system rotation is a leading-order effect. In addition we conclude that the region which is affected most by the rotation extends further to the wall with increasing rotation rate. The mean velocity of a turbulent channel flow is only weakly affected by the system rotation in the near-wall region. However, system rotation has a substantial effect on regions sufficiently far from the wall such as the logarithmic region up to the centreline.

In fact this global effect has been observed both in experiments and in DNS for the classical rotating channel flow with x_3 as the rotation axis (see e.g. Johnston *et al.* 1972; Kristoffersen & Andersson 1993). In contrast to the present case the classical rotating channel case does not reveal a symmetric mean velocity profile about the centreline. Instead a skewed mean velocity profile in the centre part of the channel is observed, which will be proven in the next subsection. This is not the case for the present flow, in which u_1 stays symmetric about the centreline.

2.2. *Reflection symmetry of statistical flow quantities about the centreline*

Reflection symmetries can be obtained by finding transformations of the form $\tilde{\phi} = -\phi$ where ϕ may represent any dependent and independent variable. The following is observed in a variety of different channel types of flow such as the usual turbulent Poiseuille and the turbulent Couette flow. If the corresponding equations and boundary conditions admit a certain reflection symmetry about the centreline, this is also verified for all statistical quantities.

For the present problem the system (2.2) and (2.5) admits the reflection symmetry where the variables are respectively separated as independent variables, mean quantities, and statistical quantities:

$$\tilde{x}_1 = x_1, \quad \tilde{x}_2 = -x_2, \quad \tilde{x}_3 = -x_3, \quad \tilde{r}_1 = r_1, \quad \tilde{r}_2 = -r_2, \quad \tilde{r}_3 = -r_3, \tag{2.11a}$$

$$\tilde{\bar{u}}_1 = \bar{u}_1, \quad \tilde{\bar{u}}_3 = -\bar{u}_3, \quad \tilde{\bar{p}} = \bar{p}, \tag{2.11b}$$

$$\begin{pmatrix} \tilde{R}_{11} & \tilde{R}_{12} & \tilde{R}_{13} \\ \tilde{R}_{21} & \tilde{R}_{22} & \tilde{R}_{23} \\ \tilde{R}_{31} & \tilde{R}_{32} & \tilde{R}_{33} \end{pmatrix} = \begin{pmatrix} R_{11} & -R_{12} & -R_{13} \\ -R_{21} & R_{22} & R_{23} \\ -R_{31} & R_{32} & R_{33} \end{pmatrix}, \tag{2.11c}$$

$$\begin{pmatrix} \widetilde{\overline{pu_1}} \\ \widetilde{\overline{pu_2}} \\ \widetilde{\overline{pu_3}} \end{pmatrix} = \begin{pmatrix} \overline{pu_1} \\ -\overline{pu_2} \\ -\overline{pu_3} \end{pmatrix}, \quad \begin{pmatrix} \widetilde{\overline{u_1 p}} \\ \widetilde{\overline{u_2 p}} \\ \widetilde{\overline{u_3 p}} \end{pmatrix} = \begin{pmatrix} \overline{u_1 p} \\ -\overline{u_2 p} \\ -\overline{u_3 p} \end{pmatrix}. \tag{2.11d}$$

These reflection symmetries can be generalized such that any other statistical one-, two-, and multi-point quantity can be determined from the fluctuation quantities according to the transformation for the fluctuations

$$\tilde{u}_1 = u_1, \quad \tilde{u}_2 = -u_2, \quad \tilde{u}_3 = -u_3, \quad \tilde{p} = p. \tag{2.12}$$

For example, the transformation of the two-point triple correlations $R_{(ik)j}$ and $R_{i(jk)}$ which are not stated above can be determined in a similar manner.

From (2.11*b*) it can be determined that $\bar{u}_1$ is symmetric about the centreline and $\bar{u}_3$ is antisymmetric about the centreline.

The transformation of the Reynolds stress tensor can also be obtained by employing equation (2.4) in the transformation (2.11*c*). The consequences for the stresses are such that all normal stresses and the off-diagonal component $\overline{u_2 u_3}$ are symmetric about the centreline. In contrast $\overline{u_1 u_2}$ and $\overline{u_1 u_3}$ are antisymmetric about the centreline. It should be noted that the results for $\overline{u_1 u_2}$ and $\overline{u_2 u_3}$ can also be obtained from the mean momentum equations (2.1*a*) and (2.1*c*). The reflection properties of other one-point

quantities such as the pressure–strain correlation and the dissipation tensor can also be determined by equation (2.12).

2.3. *Lie group analysis of the two-point correlation equation*

For simplicity it will be assumed in the following analysis that the Reynolds number tends to infinity so that the viscous terms in the two-point correlation equation (2.2) may be neglected. The basis for this assumption is the fact that, to leading order only, viscosity has no effect as $Re \to \infty$. Viscosity only affects the small scales of $\mathcal{O}(\eta)$ where η is the Kolmogorov length scale. Hence neglecting viscosity is only valid for $|\boldsymbol{r}| > \eta$. If $|\boldsymbol{r}| < \eta$, the last term of the third line in equation (2.2) corresponds to the dissipation and cannot be neglected. A rigorous asymptotic analysis of the two regions $|\boldsymbol{r}| > \eta$ and $|\boldsymbol{r}| < \eta$, i.e. the derivation of a small- and a large-scale equations, may be taken from Oberlack (2002) or Oberlack & Guenther (2003).

The general purpose of Lie group analysis, also called symmetry analysis, is two-fold. First, the symmetry transformations are determined, which give profound knowledge of the flow physics. Second, the symmetries may be used to achieve self-similarity or reduction of the two-point correlation equation. The first step to accomplish this objective is to find symmetry transformations which do not change the form of the equation under investigation. In fact, this is analogous to the analysis presented in the previous subsection where reflection symmetries have been investigated which do not alter the equations. However, the main difference in the present subsection is that the transformations considered therein are *finite* groups. In order to obtain a reduction, *continuous* groups of transformations need to be considered. The method to find the desired continuous groups of transformations is called Lie group analysis. A good introduction to this method is given in Bluman & Kumei (1989) and Stephani (1989). In the present subsection only a heuristic approach will be presented while some more mathematical details on group methods are presented in Appendix B in Oberlack (2001).

Self-similarity or reduction is always associated with the decrease of the number of independent variables. It is important to note that the independent variables are not necessarily restricted to the usual variables such as space and time. Instead any parameter in the equation under investigation may be considered as an independent variable as long as it does not implicitly depend on any other independent parameter in the problem.

Hence, in the first step a reduction will be achieved by rewriting the two-point correlation equation such that $\Omega_1 \equiv \Omega$ is absorbed into all the remaining independent and dependent variables. The most general form of transformation allowing this reduction is

$$x_i = \tilde{x}_i \gamma(\Omega), \quad r_i = \tilde{r}_i \gamma(\Omega), \quad \bar{u}_i = \tilde{\bar{u}}_i \gamma(\Omega)\Omega, \tag{2.13a}$$

$$R_{ij} = \tilde{R}_{ij}\gamma(\Omega)^2\Omega^2, \quad \overline{pu_i} = \widetilde{\overline{pu_i}}\gamma(\Omega)^3\Omega^3, \quad \overline{u_i p} = \widetilde{\overline{u_i p}}\gamma(\Omega)^3\Omega^3, \tag{2.13b}$$

$$R_{(ik)j} = \tilde{R}_{(ik)j}\gamma(\Omega)^3\Omega^3, \quad R_{i(jk)} = \tilde{R}_{i(jk)}\gamma(\Omega)^3\Omega^3, \tag{2.13c}$$

where the new variables are denoted by tilde, and $\gamma(\Omega)$ is an arbitrary function of Ω. After employing (2.13*a*)–(2.13*c*) and imposing the high-Reynolds-number limit, the two-point correlation equations are

$$\begin{aligned} 0 = &- \tilde{R}_{2j}\delta_{i1}\frac{\mathrm{d}\tilde{\bar{u}}_1(\tilde{x}_2)}{\mathrm{d}\tilde{x}_2} - \tilde{R}_{2j}\delta_{i3}\frac{\mathrm{d}\tilde{\bar{u}}_3(\tilde{x}_2)}{\mathrm{d}\tilde{x}_2} - \tilde{R}_{i2}\delta_{j1}\frac{\mathrm{d}\tilde{\bar{u}}_1(\tilde{x}_2+r_2)}{\mathrm{d}(\tilde{x}_2+\tilde{r}_2)} - \tilde{R}_{i2}\delta_{j3}\frac{\mathrm{d}\tilde{\bar{u}}_3(\tilde{x}_2+r_2)}{\mathrm{d}(\tilde{x}_2+\tilde{r}_2)} \\ &- [\tilde{\bar{u}}_1(\tilde{x}_2+\tilde{r}_2) - \tilde{\bar{u}}_1(\tilde{x}_2)]\frac{\partial \tilde{R}_{ij}}{\partial \tilde{r}_1} - [\tilde{\bar{u}}_3(\tilde{x}_2+\tilde{r}_2) - \tilde{\bar{u}}_3(\tilde{x}_2)]\frac{\partial \tilde{R}_{ij}}{\partial \tilde{r}_3} \end{aligned}$$

$$-\frac{1}{\rho}\left[\delta_{i2}\frac{\partial\widetilde{pu_j}}{\partial\tilde{x}_2}-\frac{\partial\widetilde{pu_j}}{\partial\tilde{r}_i}+\frac{\partial\widetilde{u_i p}}{\partial\tilde{r}_j}\right]$$

$$-\frac{\partial\tilde{R}_{(i2)j}}{\partial\tilde{x}_2}+\frac{\partial}{\partial\tilde{r}_k}\left[\tilde{R}_{(ik)j}-\tilde{R}_{i(jk)}\right]-2[e_{1li}\tilde{R}_{lj}+e_{1lj}\tilde{R}_{il}]. \tag{2.14}$$

Note that this is essentially the form of equation (2.2) with $\nu = 0$. Obviously the set of independent variables x_2, r_i, and Ω has been reduced by one. From group theory it follows (see Oberlack 2001, Appendix B) that equation (2.14) admits a further similarity reduction only for certain mean velocities which obey the equations

$$[a_1(\tilde{x}_2+\tilde{r}_2)+a_3+a_5]\frac{\mathrm{d}\tilde{\tilde{u}}_1(\tilde{x}_2+\tilde{r}_2)}{\mathrm{d}(\tilde{x}_2+\tilde{r}_2)}-a_1\tilde{\tilde{u}}_1(\tilde{x}_2+\tilde{r}_2)$$

$$=[a_1\tilde{x}_2+a_5]\frac{\mathrm{d}\tilde{\tilde{u}}_1(\tilde{x}_2)}{\mathrm{d}\tilde{x}_2}-a_1\tilde{\tilde{u}}_1(\tilde{x}_2), \tag{2.15a}$$

$$[a_1(\tilde{x}_2+\tilde{r}_2)+a_3+a_5]\frac{\mathrm{d}\tilde{\tilde{u}}_3(\tilde{x}_2+\tilde{r}_2)}{\mathrm{d}(\tilde{x}_2+\tilde{r}_2)}-a_1\tilde{\tilde{u}}_3(\tilde{x}_2+\tilde{r}_2)$$

$$=[a_1\tilde{x}_2+a_5]\frac{\mathrm{d}\tilde{\tilde{u}}_3(\tilde{x}_2)}{\mathrm{d}\tilde{x}_2}-a_1\tilde{\tilde{u}}_3(\tilde{x}_2). \tag{2.15b}$$

The corresponding similarity variables are obtained from the invariant surface condition (e.g. see Bluman & Kumei 1989)

$$\frac{\mathrm{d}\tilde{r}_1}{a_1\tilde{r}_1+a_2}=\frac{\mathrm{d}\tilde{r}_2}{a_1\tilde{r}_2+a_3}=\frac{\mathrm{d}\tilde{r}_3}{a_1\tilde{r}_3+a_4}=\frac{\mathrm{d}\tilde{x}_2}{a_1\tilde{x}_2+a_5}$$

$$=\frac{\mathrm{d}\tilde{R}_{ij}}{2a_1\tilde{R}_{ij}}=\frac{\mathrm{d}\widetilde{pu_i}}{3a_1\widetilde{pu_i}}=\frac{\mathrm{d}\widetilde{u_j p}}{3a_1\widetilde{u_j p}}=\frac{\mathrm{d}\tilde{R}_{(ik)j}}{3a_1\tilde{R}_{(ik)j}}=\frac{\mathrm{d}\tilde{R}_{i(jk)}}{3a_1\tilde{R}_{i(jk)}}, \tag{2.16}$$

where the constants of integration are taken as the new variables. The equations for the mean velocities (2.15*a*) and (2.15*b*) can only have a unique solution if

$$a_3 = 0. \tag{2.17}$$

Since each equation (2.15*a*) and (2.15*b*) depends on the left-hand side on $\tilde{x}_2+\tilde{r}_2$ and on the right-hand side on $\tilde{x}_2$, they can only be equal if they are both equal to a constant. Hence, by comparing the first brackets on the left and right sides respectively, equations (2.15*a*) and (2.15*b*) uniquely become

$$[a_1\tilde{x}_2+a_5]\frac{\mathrm{d}\tilde{\tilde{u}}_1(\tilde{x}_2)}{\mathrm{d}\tilde{x}_2}-a_1\tilde{\tilde{u}}_1(\tilde{x}_2)=c_1, \tag{2.18a}$$

$$[a_1\tilde{x}_2+a_5]\frac{\mathrm{d}\tilde{\tilde{u}}_3(\tilde{x}_2)}{\mathrm{d}\tilde{x}_2}-a_1\tilde{\tilde{u}}_3(\tilde{x}_2)=c_3. \tag{2.18b}$$

Each of the parameters a_1–a_5 has a distinct physical meaning. The parameter a_1 corresponds to the scaling group; i.e. equation (2.14) admits a transformation of the form

$$\tilde{x}_2^*=\mathrm{e}^{a_1}\tilde{x}_2,\quad \tilde{r}_i^*=\mathrm{e}^{a_1}\tilde{r}_i,\quad \tilde{\tilde{u}}_i^*=\mathrm{e}^{a_1}\tilde{\tilde{u}}_i, \tag{2.19a}$$

$$\tilde{R}_{ij}^*=\mathrm{e}^{2a_1}\tilde{R}_{ij},\quad \widetilde{pu_i}^*=\mathrm{e}^{3a_1}\widetilde{pu_i},\quad \widetilde{u_i p}^*=\mathrm{e}^{3a_1}\widetilde{u_i p}, \tag{2.19b}$$

$$\tilde{R}_{(ik)j}^*=\mathrm{e}^{3a_1}\tilde{R}_{(ik)j},\quad \tilde{R}_{i(jk)}^*=\mathrm{e}^{3a_1}\tilde{R}_{i(jk)}, \tag{2.19c}$$

which does not alter the functional form of the equation written in the new coordinates. The parameters a_2–a_5 correspond to the translation groups which conform to the fact that (2.14) is autonomous with respect to $\tilde{x}_2$ and $\tilde{r}_i$. As a result (2.14) is invariant under transformations such as

$$\tilde{x}_2^* = \tilde{x}_2 + a_5. \tag{2.20}$$

However, for physical reasons the translation invariance of $\tilde{r}_i$ is not meaningful, and a_2–a_4 must be zero. In order to understand the problem with these 'artificial' invariances, one has to call to mind that the translation invariance with respect to $\tilde{r}_i$ gives rise to a new solution where the correlation function is shifted in correlation space. Since R_{ij} reaches its finite maximum at $|\tilde{\boldsymbol{r}}| = 0$ and tends to zero for $|\tilde{\boldsymbol{r}}| \to \pm\infty$, a shift in the correlation space cannot be a new solution.

Depending on the value of a_1, two fundamentally different cases are to be distinguished for which a similarity reduction may be obtained.

2.3.1. $a_1 \neq 0$

This case corresponds to the fact that scaling with respect to space is not inhibited and (2.18*a*) and (2.18*b*) integrate to

$$\tilde{\bar{u}}_1 = C_1(\bar{x}_2 + a_5/a_1) - c_1/a_1, \tag{2.21a}$$

$$\tilde{\bar{u}}_3 = C_3(\bar{x}_2 + a_5/a_1) - c_3/a_1, \tag{2.21b}$$

where C_1 and C_3 are integration constants. If the transformation (2.13*a*) to the original coordinates is inferred, equations (2.21) become

$$\bar{u}_1 = C_1\,\Omega\,x_2 + \Omega\,\gamma(\Omega)(C_1 a_5/a_1 - c_1/a_1), \tag{2.22a}$$

$$\bar{u}_3 = C_3\,\Omega\,x_2 + \Omega\,\gamma(\Omega)(C_3 a_5/a_1 - c_3/a_1). \tag{2.22b}$$

It appears that the additive constants may depend on the rotation rate in an unknown manner. In order to resolve this problem, it is helpful to investigate the two-point correlation function.

Though a solid theoretical basis on first principles is still lacking, it appears from the present DNS computations that to leading order the two-point correlation function does not scale with the rotation rate Ω. This is an empirical observation from DNS data, that R_{ij} is only very weakly influenced. Hence it can be concluded from equation (2.13*b*) that, in order to have no Ω dependence of R_{ij}, the function γ behaves as $\gamma \sim 1/\Omega$. As a result, the two additive constants appearing in the scaling laws (2.22*a*) and (2.22*b*) do not depend on Ω either. Only the slope of the linear scaling laws depends on the rotation rate.

The similarity variables for the case $a_1 \neq 0$ corresponding to the mean velocities (2.21*a*) and (2.21*b*) are obtained from the characteristic equations (2.16). Employing $a_2 = a_3 = a_4 = 0$, the integration yields

$$\eta_1 = \frac{\tilde{r}_1}{\tilde{x}_2 + a_5/a_1}, \quad \eta_2 = \frac{\tilde{r}_2}{\tilde{x}_2 + a_5/a_1}, \quad \eta_3 = \frac{\tilde{r}_3}{\tilde{x}_2 + a_5/a_1}, \tag{2.23a}$$

$$\tilde{R}_{ij} = F_{ij}(\tilde{x}_2 + a_5/a_1)^2, \quad \widetilde{\overline{pu_i}} = G_i(\tilde{x}_2 + a_5/a_1)^3, \widetilde{\overline{u_j p}} = H_j(\tilde{x}_2 + a_5/a_1)^3, \tag{2.23b}$$

$$\tilde{R}_{(ik)j} = F_{(ik)j}(\tilde{x}_2 + a_5/a_1)^3, \quad \tilde{R}_{i(jk)} = F_{i(jk)}(\tilde{x}_2 + a_5/a_1)^3, \tag{2.23c}$$

where the integration constants η_i, F_{ij}, G_i, H_i, $F_{(ik)j}$, and $F_{i(jk)}$ are the new similarity variables. In order to verify the similarity reduction of equation (2.14), the quantities F_{ij}, G_i, H_i, $F_{(ik)j}$, and $F_{i(jk)}$ are introduced as new dependent variables only depending on η_i.

In order to obtain a new identity in similarity space, the latter scaling is substituted into equation (2.6) for R_{ij}. For this purpose the origin of $\tilde{x}_2$ may be chosen as

$$\tilde{x}_2' = \tilde{x}_2 + \frac{a_5}{a_1} \tag{2.24}$$

such that the similarity variable simplifies to

$$\eta_i = \frac{\tilde{r}_i}{\tilde{x}_2'}. \tag{2.25}$$

Introducing the transformations (2.23*a*)–(2.23*c*) into equation (2.6), we obtain the relation $F_{ij}(\tilde{x}_2', \tilde{x}_2'\boldsymbol{\eta})(\tilde{x}_2')^2 = F_{ji}(\tilde{x}_2'(1+\eta_2), -\tilde{x}_2'\boldsymbol{\eta})\,(\tilde{x}_2')^2$. Since it was previously assumed that all two-point correlation functions are solely functions of $\boldsymbol{\eta}$, only the ratio of the first and the second parameter can appear in F_{ij}. Thus, we finally obtain

$$F_{ij}(\boldsymbol{\eta}) = F_{ji}\left(\frac{-\boldsymbol{\eta}}{1+\eta_2}\right). \tag{2.26}$$

This relation gives valuable insight into the structure of the solution and it connects different $\tilde{\boldsymbol{r}}$ domains to each other.

Interestingly, relation (2.26) gives raise to a new symmetry transformation

$$\tilde{\eta}_i = \frac{-\eta_i}{1+\eta_2} \tag{2.27}$$

which is neither a reflection symmetry in the classical sense nor a continuous transformation (Lie group) since it does not contain a continuous parameter. Its validity can be verified by substituting (2.27) into (2.14) after the similarity coordinate (2.25) and the linear profiles (2.21*a*) and (2.21*b*) have been employed.

Another interesting feature of (2.26) is that it can be considered as an algebraic functional equation for the trace element of F_{ij} or R_{ij} in the following, denoted as $F_{[ii]}$ with $i = 1, 2, 3$. The 'equilibrium' plane for (2.26) is $\eta_2 = -2$ with arbitrary η_1 and η_3 where both the argument and the value of F_{ij} are the same. In addition $\boldsymbol{\eta} = 0$ is an 'equilibrium' point. Apart from these two regions, equation (2.26) defines a mapping between different $\boldsymbol{\eta}$-domains. There are two pairs of η_2-regions which map into each other, namely

$$\eta_2: \quad (-\infty, -2) \leftrightarrow (-2, -1) \quad \text{and} \quad (-1, 0) \leftrightarrow (0, \infty). \tag{2.28}$$

This nomenclature refers to the fact that, once the functional values for $F_{[ii]}$ in the η_2 region $(-2, -1)$ are known, the corresponding values in the region $(-\infty, -2)$ are uniquely determined and vice versa. After a value for η_2 is chosen, the values for η_1 and η_3 map according to

$$\frac{-\eta_1}{1+\eta_2} \rightarrow \eta_1 \quad \text{and} \quad \frac{-\eta_3}{1+\eta_2} \rightarrow \eta_3 \tag{2.29}$$

A graphical mapping scheme is given in figure 2. For clarity only the η_1, η_2 domain is depicted where connected mapping regions are indicated by arrows. The extension to the entire $\boldsymbol{\eta}$-domain is straightforward.

Besides the above symmetry relation for $F_{[ii]}$ with $i = 1, 2, 3$, equation (2.26) provides solutions for any off-diagonal F_{ij} element with $(i \neq j)$ if F_{ji} is known. Of course, similar features can be found for the pressure–velocity correlation and for the triple correlation.

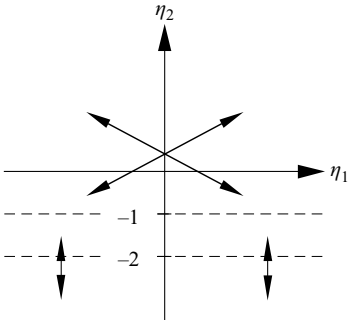

FIGURE 2. Non-locally related correlations in the (η_1, η_2)-plane according to (2.26).

For the present case $a_1 \neq 0$, the statistical variables scale with the wall distance. This is not the case in the following subsection.

2.3.2. $a_1 = 0$

This case corresponds to the scaling with respect to space being broken as can also be read from (2.19*a*)–(2.19*c*). As a result equation (2.18*a*) and (2.18*b*) may be integrated to

$$\tilde{\tilde{u}}_1 = \frac{c_1}{a_5}\tilde{x}_2 + C_3, \quad \tilde{\tilde{u}}_3 = \frac{c_3}{a_5}\tilde{x}_2 + C_4, \tag{2.30a, b}$$

where C_3 and C_4 are integration constants. The characteristic equation (2.16) cannot be integrated in the usual way. However, a reduction may still be possible since the correlation equation is autonomous with respect to x_2. Due to the linear profile all statistical functions in equation (2.14) may not depend on the spatial coordinate $\tilde{x}_2$. Obviously, the present case corresponds to a homogeneous shear flow. Even though this does not appear to be a reduction in the usual sense from a group theoretical point of view, this is similar to the case $a_1 \neq 0$. In § 2.3.1 a reduction was attained by the scaling group (a_1) while in the present case the reduction may be attained by the translation group (a_5). In both cases the dimensionality of the problem is reduced.

It should be noted that for physical reasons the case $a_1 \neq 0$ appears to be more likely to be applicable to the rotating channel flow for the following reason. One of the key observations in Oberlack (2001) was that turbulence has a tendency to establish a maximum degree of symmetry transformation. For the different channel flow cases, the highest degree of symmetry has been observed where the least wall influence is present, namely in the core region of the channel. Hence it may be expected that the same maximum principle applies for the present flow.

It is very important to note that the present analyses, in particular in §§ 2.3.1 and 2.3.2, are not limited to the two-point correlation equation. The results regarding all the symmetries and scaling laws hold for all multi-point correlation equations to arbitrary order. Hence the closure problem of turbulence which usually precludes exact results is not an obstacle for the present analysis.

More mathematical details on group methods and how to obtain the above results can be found in appendix B of Oberlack (2001).

To conclude from the analysis, it is to be expected that a cone-shaped mean velocity in the streamwise direction will appear such that the two flanks of the cone are linear. Furthermore, linear profiles for the cross-flow will also be established on both sides of the centreline.

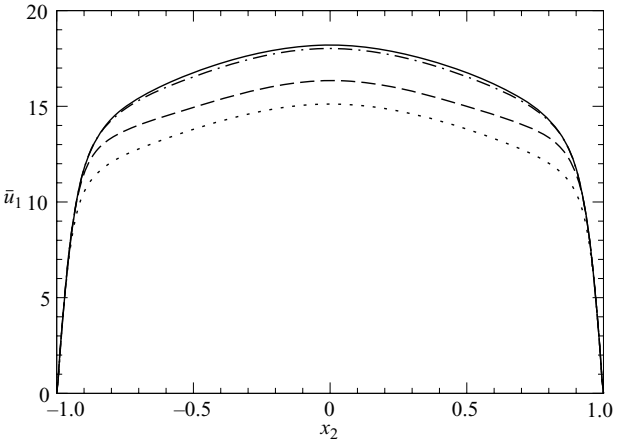

FIGURE 3. Streamwise mean velocity at $Ro = 0$ (———), $Ro = 2.5$ (— · —), $Ro = 6.5$ (– – – –), and $Ro = 10$ (· · · · · ·).

3. Direct numerical simulation of the flow

The numerical technique used is a standard spectral method with Fourier decomposition in the streamwise and spanwise directions and a Chebyshev decomposition in the wall-normal direction. The original version of the numerical code was developed at KTH/Stockholm by Lundbladh, Henningson & Johanson (1992). Additional features such as the streamwise rotation and statistics were added during the project. All flow quantities are non-dimensionalized by $h/2$ and u_τ where h is the channel width and u_τ is the friction velocity of the fully developed turbulent flow field. The boundary conditions are non-slip at $x_2 = \pm 1$ and periodic in the x_1- and x_3-directions. For all computations the pressure gradient is kept constant. Further details on the numerical scheme may be obtained from Lundbladh *et al.* (1992).

After the simulations were finalized all flow quantities were normalized on the friction velocity u_τ. The definition of the Reynolds number and its numerical value for all subsequent calculations below are

$$Re_\tau = \frac{hu_\tau}{2\nu} = 180. \tag{3.1}$$

The rotation number is defined as

$$Ro = \frac{\Omega h}{u_\tau}. \tag{3.2}$$

Four computations at rotation numbers $Ro = 0$, 2.5, 6.5 and 10 have been conducted. All results presented for $Ro = 0$ are in good agreement with the data from Kim, Moin & Moser (1987). The domain sizes used in the x_1, x_2, and x_3-directions are 4π, 2, and 2π on $128 \times 129 \times 128$ grids, respectively, for the $Ro = 0$, 2.5 and 6.5 cases, and 8π, 2, and 4π on a $256 \times 129 \times 128$ grid for the $Ro = 10$ case. In figure 3 the streamwise mean velocity profiles at $Ro = 0$, 2.5, 6.5, and 10 are compared. As expected from the global time-scale analysis, the near-wall region up to $x_2 = \pm 0.9$ is only marginally perturbed. Approaching the core region of the flow, a significant change in the mean velocity profile is visible with a very pronounced shoulder at $x_2 = \pm 0.8$ for $Ro = 10$. In addition, a much flatter centre region is noticeable. It is interesting to note that a decrease of mass flow is induced by the rotation.

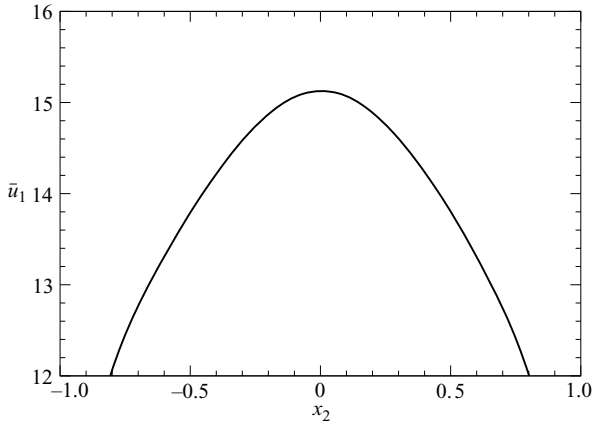

FIGURE 4. Streamwise mean velocity at $Ro = 10$ in the core region.

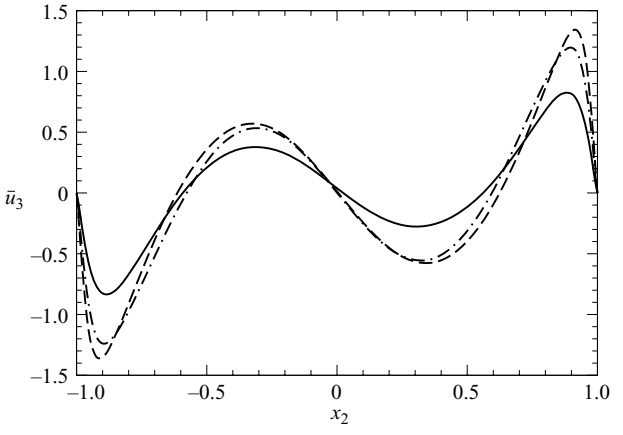

FIGURE 5. Spanwise mean velocity at $Ro = 2.5$ (———), $Ro = 6.5$ (— · —), and $Ro = 10$ (– – – –).

As predicted by the group analysis, two linear regions appear to emerge on each side of the centreline for the high rotation rate. A more detailed perspective of the linear region is given in figure 4 where only the 'head' of the profile for $Ro = 10$ is depicted. The linear regions roughly cover the wide range $x_2 = 0.2$–0.6 on both sides of the centreline.

As already mentioned in § 2, a mean cross-flow denoted by $\bar{u}_3$ is induced by the rotation. In § 2.2 it was predicted that the flow is skew-symmetric about the centerline as shown in figure 5.

Though a clearer verification is still lacking, it appears that the predicted linear profile is also visible in the induced cross-flow. The location of the linear region is slightly shifted towards the wall region compared to the linear region of the streamwise velocity. One of the most interesting features of the cross flow is the region near the centreline. There the cross-flow has opposite sign compared to the flow regions closer to the channel walls. The source of this effect is not fully understood yet, though it appears unlikely that it is a large-scale property of the flow since no such flow pattern

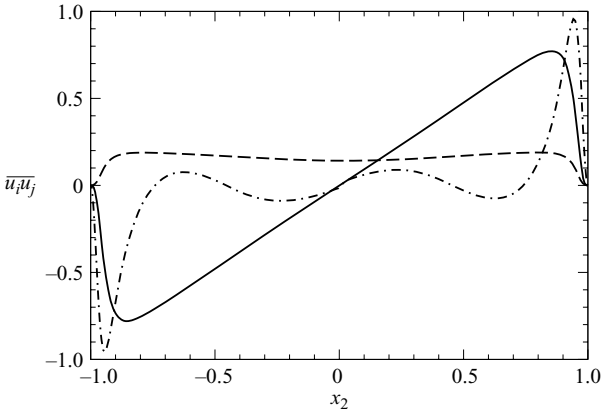

FIGURE 6. Shear stresses at $Ro = 10$: $\overline{u_1 u_2}$ (———), $\overline{u_2 u_3}$ (– – – –), $\overline{u_1 u_3}$ (— · —).

was seen in the flow visualization. Note that for low rotation rates the mean spanwise velocity profiles increase, but appear to decrease for higher rotation rates.

From the statistical one-point quantities, only the Reynolds stress tensor has been computed. In figure 6 the Reynolds shear stresses at $Ro = 10$ are displayed. Both the linear and the constant curves for $\overline{u_1 u_2}$ and $\overline{u_2 u_3}$ respectively can be derived from equations (2.1*a*) and (2.1*c*) by neglecting the viscous terms, which are only significant in the near-wall region. One of the most intriguing features of the shear stresses is the induced $\overline{u_1 u_3}$ component. The two other cross-stresses can both be interpreted in terms of a simplified eddy-viscosity model, proportional to their corresponding mean velocities. However, this cannot be done for the $\overline{u_1 u_3}$ shear stress. Hence $\overline{u_1 u_3}$ can only be modelled with the aid of more elaborate turbulence models such as LES or Reynolds stress transport models, to be presented in the next subsection.

In a corresponding DNS at $Ro = 0$, only the Reynolds shear stress $\overline{u_1 u_2}$ is non-zero. This curve is not shown in figure 6 since both $\overline{u_1 u_2}$ stress curves are very close to each other and only differ slightly in the near-wall region where viscosity is dominating the flow. All statistical curves exhibit the reflection symmetry properties about the centreline found in § 2.2.

The normal stresses for both the rotating and the non-rotating case are depicted in figure 7. Only very weak differences are noticeable compared to the strong change in the streamwise mean velocity induced by the rotation. Though the shape and magnitude of each set of curves for $Ro = 0$ and $Ro = 10$ are very similar, there are some distinct qualitative differences in the core region of the flow. We recall that the largest changes should be visible towards this core region as to be expected from the time-scale analysis.

A general problem with rotating flows is the fact that in order to obtain good statistics the required integration time of the computation is significantly longer than for the corresponding non-rotating case. Computations Ro =2.5, 6.5 and 10 were run for $550(h/2)/u_\tau$ time units and the statistics collected for the last 225 time units. The classical case, i.e. no rotation, was run for $330(h/2)/u_\tau$ time units and the statistics collected for the last 165 time units.

Also, it is observed in the rotating pipe flow computation by Orlandi & Fatica (1997) that very long coherent structures appear in the streamwise direction. This requires a very large computational box in order to ensure a sufficient decay to zero for the two-point correlation functions. For the present computation it was also

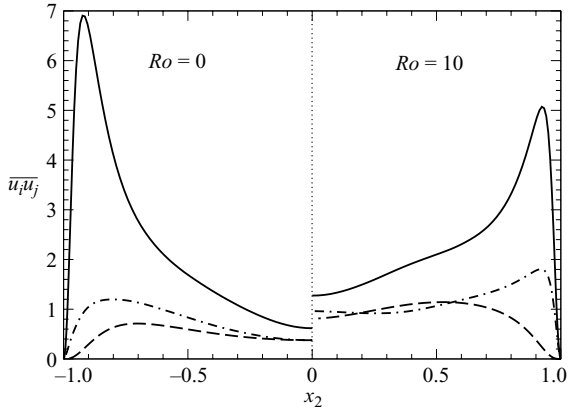

FIGURE 7. Normal stresses at $Ro = 0$ on the left and $Ro = 10$ on the right: $\overline{u_1 u_1}$ (———), $\overline{u_2 u_2}$ (– – – –), $\overline{u_3 u_3}$ (— · —).

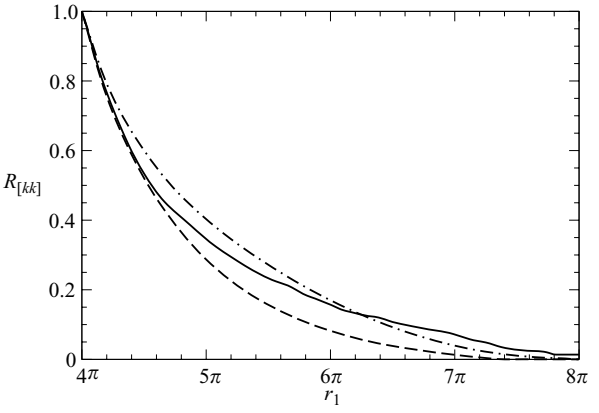

FIGURE 8. Two-point correlations in the streamwise direction at mid-plane ($x_2 = 0$) for $Ro = 10$: R_{11} (———), R_{22} (– – – –), R_{33} (— · —).

noticed that the box in the streamwise direction needs to be larger than for the non-rotating channel flow. In figure 8 the two-point correlations in the streamwise direction for all normal stresses are shown at mid-plane ($x_2 = 0$). Here all curves fall to zero, confirming that the chosen computional box is large enough.

4. Model computations

System rotation is not a singular influence on the flow, but belongs to a wider class of benchmarks which mimics mean streamline curvature. This is very important for almost any application. Since system rotation is a challenging measure for turbulence models, we have investigated the response of two classes of turbulence models to the influence of streamwise rotation on the turbulent channel flow. First, LES of turbulence has been investigated. Thereafter, a second-moment closure has been employed to test its ability to model the flow. Classical two-equation models such as the k–ε or the k–ω model have not been examined since they exhibit no sensitivity to system rotation. This deficiency can be directly deduced from the model equations

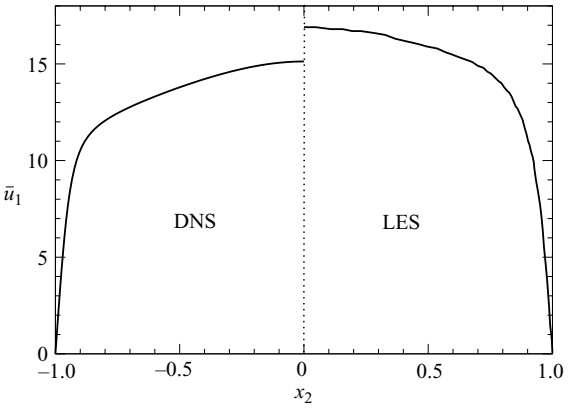

FIGURE 9. Streamwise mean velocity from DNS on the left and LES on the right at $Ro = 10$.

since no Coriolis type of term appears in the transport equation for the statistical quantities.

4.1. *Large-eddy simulations*

The first turbulence model to be investigated here is the dynamic subgrid-scale model of Germano *et al.* (1991) and Lilly (1992) used in LES. Since the dynamic model is 'two-dimensional material-frame indifferent' (see Speziale 1981; Oberlack 1997), one may expect that at least in the limit of large rotation numbers the model should capture the trends observed in the DNS. It will be seen subsequently that the dynamic model captures very well most of the trends in the flow, even quantitatively, except for the linear regions in the streamwise mean velocity. The flow parameters and the numerical scheme are the same.

The domain sizes used in the x_1-, x_2-, and x_3-directions are 4π, 2, and $4\pi/3$ on $48 \times 32 \times 32$ grids, respectively, for the $Ro = 0$ case, and 8π, 2, and 2π on a $96 \times 33 \times 48$ grid for the $Ro = 10$ case.

In figure 9 the streamwise mean velocities from DNS and LES are compared. Even though the LES profile changes significantly due to the system rotation, it does not exhibit the clear linear region observed in the DNS. In addition, the mass flux is much higher than in the DNS.

In figure 10 the shear stresses from the DNS are very well represented by the LES calculation. Even quantitatively there is close agreement with the DNS. The normal stresses in figure 11 exhibit less good agreement with the DNS, but a correct qualitative agreement is clearly visible. In particular, the near-wall peak of $\overline{u_1 u_1}$ is too high compared to the DNS.

4.2. *Reynolds-averaged modelling*

To this end the SSG second-moment closure (SMC) model (see Speziale, Sarkar & Gatski 1991) has been used in conjunction with the elliptic-relaxation approach (Durbin 1991, 1993) to model near-wall effects. The details of the model are given in Pettersson, Andersson & Brunvoll (1998). There exist a fairly large number of different second-moment closure schemes in the literature, but the one chosen here suffices to demonstrate some of the outstanding single-point modelling challenges. We have observed essentially the same behaviour using the simpler IP model (see Launder, Reece & Rodi 1975) and the more elaborate RLA model (see Ristorcelli, Lumley & Abid 1995).

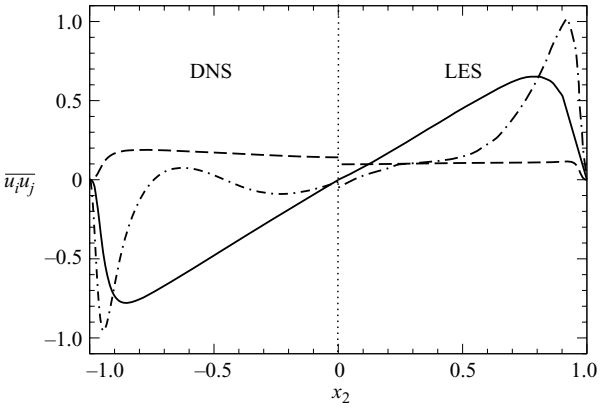

FIGURE 10. Shear stresses from the DNS on the left and LES on the right at $Ro = 10$: $\overline{u_1u_2}$ (———), $\overline{u_2u_3}$ (– – – –), $\overline{u_1u_3}$ (— · —).

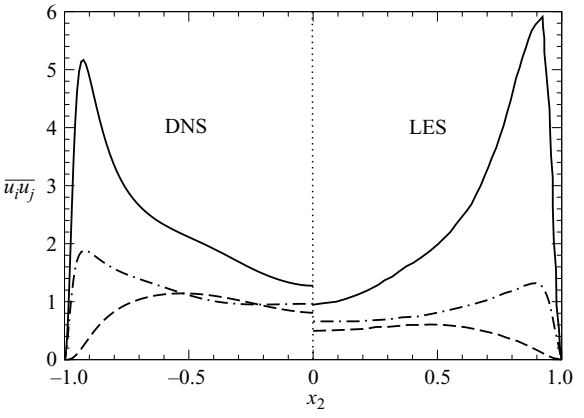

FIGURE 11. Normal stresses from the DNS on the left and LES on the right at $Ro = 10$: $\overline{u_1u_1}$ (———), $\overline{u_2u_2}$ (– – – –), $\overline{u_3u_3}$ (— · —).

A salient feature of rotating channel flow, from a modelling perspective, is that the imposed Coriolis force only indirectly affects the mean flow field. It is the turbulent stresses that are primarily affected. The response of SMC models to an imposed rotation is rather different in a streamwise rotating channel than in the more traditional channel with spanwise rotation. One distinct difference is that the response of the imposed rotation is symmetric in the former case. Except for a simple reflection the sign of Ω_k is of no importance. In a spanwise rotating channel, on the other hand, the response depends on whether the imposed rotation is cyclonic or anticyclonic, i.e. if the rotation vector is parallel or antiparallel to the mean vorticity.

The predicted distribution of the mean velocity components across the channel is shown in figures 12 and 13. Since the pressure gradient was kept constant during these computations, the bulk velocity was allowed to vary with rotation number. As can be seen in figure 12, the RANS model overpredicts the effect of rotational stabilization since the bulk velocity is overpredicted compared to the reference data (DNS and LES). The secondary mean flow component in figure 13 exhibits a somewhat different distribution than the reference data. It was observed during the course of this study that the particular distribution of $\bar{u}_3$ strongly depends on the adopted pressure–strain model.

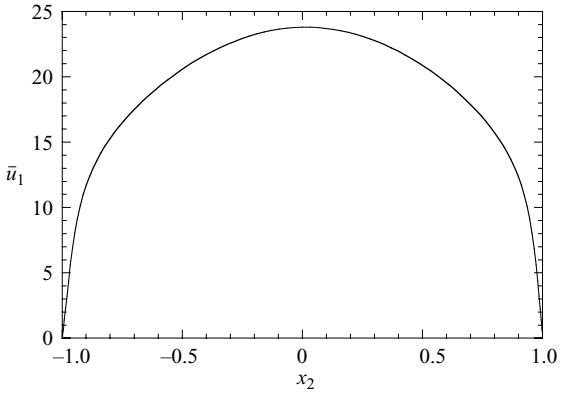

FIGURE 12. Streamwise velocity from the RANS model at $Ro = 10$.

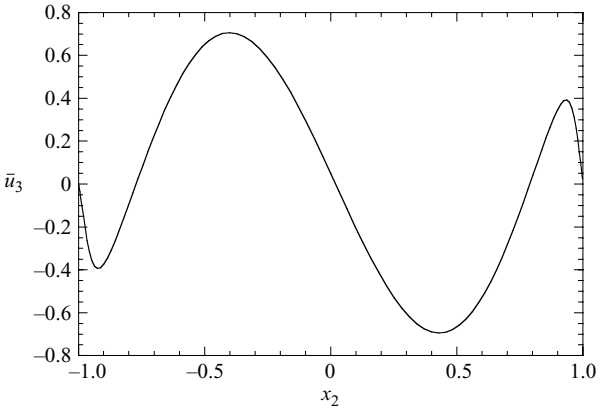

FIGURE 13. Spanwise velocity from the RANS model at $Ro = 10$.

The normal Reynolds-stress components at $Ro = 10$ are displayed in figure 14 and the results compare reasonably well with both the DNS and LES results. The off-diagonal components $\overline{u_1u_2}$ and $\overline{u_2u_3}$ of the Reynolds-stress tensor shown in figure 15 are in close agreement with the reference data. The predicted secondary shear stress $\overline{u_1u_3}$ is in significant error; even the sign is wrong compared to the LES and DNS results. Although this component is 'secondary' in that it does not affect the mean velocity field directly, it plays a significant role in the dynamics of the Reynolds-stress components.

In order to elucidate this problem, let us first consider the exact equation governing the transport of the kinematic Reynolds stress tensor $\overline{u_iu_j}$ in a non-inertial frame of reference, which can be written as

$$\frac{\partial \overline{u_iu_j}}{\partial t} + \overline{u}_k \frac{\partial \overline{u_iu_j}}{\partial x_k} = \underbrace{-\left(\overline{u_iu_k}\frac{\partial \overline{u}_j}{\partial x_k} + \overline{u_ju_k}\frac{\partial \overline{u}_i}{\partial x_k}\right)}_{P_{ij}}$$

$$\underbrace{-2\Omega_m(e_{mki}\overline{u_ju_k} + e_{mkj}\overline{u_iu_k})}_{R_{ij}} + \nu\frac{\partial^2 \overline{u_iu_j}}{\partial x_k \partial x_k} - \frac{\varepsilon}{k}\overline{u_iu_j} + \wp_{ij} - \frac{\partial \mathscr{C}_{ijk}}{\partial x_k} \quad (4.1)$$

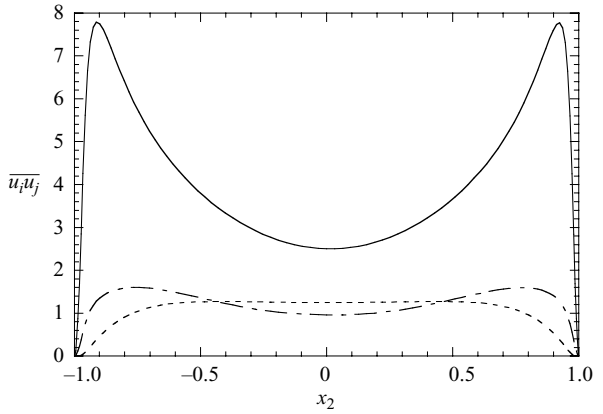

FIGURE 14. Normal stresses from the SSG model at $Ro = 10$: $\overline{u_1 u_1}$ (———), $\overline{u_2 u_2}$ (– – – –), $\overline{u_3 u_3}$ (— – —).

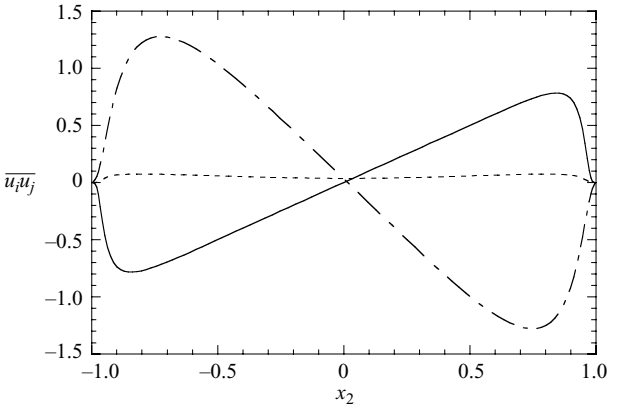

FIGURE 15. Shear stresses from the SSG model at $Ro = 10$: $\overline{u_1 u_2}$ (———), $\overline{u_2 u_3}$ (– – – –), $\overline{u_1 u_3}$ (— – —).

for an incompressible fluid, where

$$\wp_{ij} = \underbrace{-\overline{\frac{p}{\rho}\left(\frac{\partial u_i}{\partial x_j} + \frac{\partial u_j}{\partial x_i}\right)}}_{\phi_{ij}} - \varepsilon_{ij} + \frac{\varepsilon}{k}\overline{u_i u_j} \tag{4.2}$$

is a trace-less redistribution tensor, and

$$\mathscr{C}_{ijk} = \overline{u_i u_j u_k} + \frac{\delta_{ki}}{\rho}\overline{u_j p} + \frac{\delta_{kj}}{\rho}\overline{u_i p}, \tag{4.3}$$

represents turbulent and pressure diffusion. The rate of viscous dissipation is given by

$$\varepsilon_{ij} = \nu\overline{\frac{\partial u_i}{\partial x_k}\frac{\partial u_j}{\partial x_k}}$$

and ϕ_{ij} is the conventional pressure–strain correlation tensor. Here, Ω_k denotes a constant angular velocity of the reference frame about the x_k-axis. The first two terms

on the right-hand side of (4.1) represent the rate of production due to mean velocity gradient (P_{ij}) and the imposed frame rotation (R_{ij}). The only unclosed terms in (4.1) are $\wp_{ij}$ and $\mathscr{C}_{ijk}$.

An important distinction between an imposed streamwise rotation and an imposed spanwise rotation is that all components of the Reynolds stress tensor are non-zero. In the above case $\overline{u_1u_2}$ is the only non-zero off-diagonal component of the Reynolds stress tensor. It is particularly challenging in the present case since the primary shear stress, which is ultimately responsible for changes of the streamwise mean velocity field, is directly affected by the imposed rotation only through one of the secondary shear stress components, i.e.

$$R_{12} = 2\Omega_1\overline{u_1u_3} \tag{4.4}$$

(there are of course indirect effects of rotation through the other components of the Reynolds stress tensor). The situation is made even more subtle by recalling that it is the imposed rotation Ω_1 that alone is responsible for a non-zero value of $\overline{u_1u_3}$. It should also be recalled from (4.1) that the imposed rotation enters the set of governing equations implicitly through the fluctuating pressure which is part of the pressure–strain correlation tensor. Modelling of the pressure–strain term is therefore of crucial importance. The SSG model constitutes the most general linear pressure–strain model and it comprises all major building blocks of state-of-the-art RANS closures.

Stabilization of turbulence due to the imposed rotation in the model computations is essentially determined by the sum

$$R_{12} + (\phi_{12})_\Omega = \left(1 - \frac{C_2}{2}\right) R_{12} \tag{4.5}$$

if the simpler IP model (Launder *et al.* 1975) is used for convenience. Here, $(\phi_{12})_\Omega$ denotes the rotational part of the pressure–strain term. The model thus indicates that the exact term R_{12} is responsible for the suppression of $\overline{u_1u_2}$ because $\overline{u_1u_2}$ and $\overline{u_1u_3}$ have opposite signs. The rapid pressure–strain term, on the other hand, is counteracting that effect since $C_2 > 0$. The DNS and LES data however show the opposite, namely that it must be the pressure–strain correlation term ϕ_{12} that is responsible for the stabilization of $\overline{u_1u_2}$ (because both $\overline{u_1u_2}$ and $\overline{u_1u_3}$ have the same sign). The apparent success of the SMC models to predict the observed reduction of $\overline{u_1u_2}$ due the imposed streamwise rotation, although the rotational effect is overpredicted, is therefore not a result of a good pressure–strain model, but rather of another striking failure: the incorrect sign of secondary shear stress component $\overline{u_1u_3}$. This is sometimes referred to as the '$\overline{u_1u_3}$-anomaly' (e.g. see Jakirlic, Hanjalic & Tropea 2000).

5. Summary and conclusions

The general purpose of the present work is to establish a new but still very simple canonical test case to study basic turbulence physics. It has been confirmed by DNS that there are linear regions in both the streamwise and the spanwise mean velocity as was suggested by Lie group analysis of the two-point correlation equations. Additional scaling properties of the two-point correlation functions have been established.

Beside the mean flow, all Reynolds-stress quantities have been computed. In contrast to the classical rotating channel flow, all six Reynolds stress components are non-zero.

The stress components from the DNS have the expected symmetry properties about the centreline as predicted by the symmetry analysis.

The flow is very challenging for turbulence models since common two-equation models cannot account for the rotation effects. Both LES with the dynamic subgrid-scale model and second-moment models have been tested for the present flow geometry. The LES captures most of the DNS results very well. Only the linear regions in the streamwise velocity were not visible. A second-moment model captured some basic trends of the flow. However, several serious drawbacks have been encountered, and it is rather disturbing that the apparent success of the RANS model is not founded on a physically appealing closure formulation. The most serious issue is related to the secondary shear-stress component $\overline{u_1 u_3}$ which is predicted with the wrong sign. This erroneous behaviour has been traced to the important pressure–strain correlation model.

REFERENCES

Bluman, G. W. & Kumei, S. 1989 *Symmetries and Differential Equations*. Springer.

Durbin, P. 1991 Near-wall turbulence closure modeling without 'damping functions'. *Theor. Comput. Fluid Dyn.* **3**, 1–13.

Durbin, P. 1993 A Reynolds stress model for near-wall turbulence. *J. Fluid Mech.* **249**, 465–498.

Germano, M., Piomelli, U., Moin, P. & Cabot, W. 1991 A dynamic subgrid-scale eddy viscosity model. *Phys. Fluids* A **3**, 1760–1765.

Hinze, J. O. 1987 *Turbulence*. McGraw-Hill.

Jakirlic, S., Hanjalic, K. & Tropea, C. 2000 Second-moment closure analysis of rotating and swirling confined flows. In *European Congress on Computational Methods in Applied Sciences and Engineering, Barcelona, 11–14 September*, pp. 1–24. ECCOMAS.

Johnston, J. P., Halleen, R. M. & Lazius, D. K. 1972 Effects of spanwise rotation on the structure of two-dimensional fully developed turbulent channel flow. *J. Fluid Mech.* **56**, 533–557.

Kim, J., Moin, P. & Moser, R. 1987 Turbulence statistics in fully developed channel flow at low Reynolds number. *J. Fluid Mech.* **177**, 133–166.

Kristoffersen, R. & Andersson, H. I. 1993 Direct simulations of low-Reynolds-number turbulent flow in a rotating channel. *J. Fluid Mech.* **256**, 163–197.

Launder, B. E., Reece, G. E. & Rodi, W. 1975 Progress in the development of Reynolds-stress turbulence closure. *J. Fluid Mech.* **68**, 537–566.

Lilly, D. K. 1992 A proposed modification of the Germano subgrid-scale closure method. *Phys. Fluids* A **4**, 633–635.

Lundbladh, A., Henningson, D. & Johanson, A. 1992 An efficient spectral integration method for the solution of the Navier-Stokes equations. *Tech. Rep.* FFA-TN 1992-28. Aeronautical Research Institute of Sweden, Bromma.

Oberlack, M. 1994 Herleitung und Lösung einer Längenmaß- und Dissipations-Tensorgleichung für turbulente Strömungen. PhD thesis, Inst. f. Techn. Mechanik, RWTH Aachen.

Oberlack, M. 1995 Analysis of the two-point velocity correlations in turbulent boundary layer flows. In *Annual Research Briefs* (ed. P. Moin), pp. 209–220. Center for Turbulence Research, Stanford University/NASA Ames, CA, USA.

Oberlack, M. 1997 Invariant modelling in large-eddy simulation of turbulence. In *Annual Research Briefs* (ed. P. Moin), pp. 3–22. Center for Turbulence Research, Stanford University/NASA Ames, CA, USA.

Oberlack, M. 2001 Unified approach for symmetries in plane parallel turbulent shear flows. *J. Fluid Mech.* **427**, 299–328.

Oberlack, M. 2002 *Symmetries and Invariant Solutions of Turbulent Flows and their Implications for Turbulence Modelling*, pp. 301–366. Springer.

Oberlack, M. & Guenther, S. 2003 Shear-free turbulent diffusion – classical and new scaling laws. *Fluid Dyn. Res.* **33**, 453–476.

Orlandi, P. & Fatica, M. 1997 Direct simulations of turbulent flow in a pipe rotating about its axis. *J. Fluid Mech.* **343**, 43–72.

Pettersson, B. A., Andersson, H. I. & Brunvoll, A. S. 1998 Modeling near-wall effects in axially rotating pipe flow by elliptic relaxation. *AIAA J.* **36**, 1164–1170.

Ristorcelli, J. R., Lumley, J. L. & Abid, R. 1995 A rapid-pressure covariance representation consistent with the Taylor-Proudman theorem materially frame indifferent in the two-dimensional limit. *J. Fluid Mech.* **292**, 111–152.

Rotta, J. C. 1972 *Turbulente Strömungen.* Teubner, Stuttgart.

Speziale, C. G. 1981 Some interesting properties of two-dimensional turbulence. *Phys. Fluids* **28**, 1425–1427.

Speziale, C. G., Sarkar, S. & Gatski, T. 1991 Modelling the pressure–strain correlation of turbulence: an invariant dynamical systems approach. *J. Fluid Mech.* **227**, 245–272.

Stephani, H. 1989 *Differential Equations: Their Solution Using Symmetries* (ed. M. MacCallum). Cambridge University Press.